2023-07-30

Characterization of uncertainty in maximum tidal elevation near Bangladesh coastline due to uncertain sea level rise

Sarwar, S

10.1111/jfr3.12935
Journal of Flood Risk Management
Wiley

Characterisation of uncertainty in maximum tidal elevation near Bangladesh coastline due to uncertain sea level rise

Sifat Sarwar[a,b,1,*], Alistair G.L. Borthwick[c,d]

[a]Architecture Discipline, Science, Engineering and Technology School, Khulna University, Khulna 9208, Bangladesh. ORCID ID: https://orcid.org/0000-0002-7334-6710

[b]Institute for Energy Systems, School of Engineering, The University of Edinburgh, The King's Buildings, Edinburgh, UK, EH9 3JL.

[c]Institute for Infrastructure and Environment, School of Engineering, The University of Edinburgh, The King's Buildings, Edinburgh, UK, EH9 3JL. ORCID ID: https://orcid.org/0000-0001-6053-7764

[d]School of Engineering, Computing and Mathematics, University of Plymouth, Drake Circus, Plymouth, UK, PL4 8AA.

*Corresponding author:

Sifat Sarwar

ORCID ID: https://orcid.org/0000-0002-7334-6710
Email: sifatsarwar@arch.ku.ac.bd
Tel: +880 1321 571519

[1] Present address: Architecture Discipline, Science, Engineering and Technology School, Khulna University, Khulna 9208, Bangladesh

Characterisation of uncertainty in maximum tidal elevation near Bangladesh coastline due to uncertain sea level rise

Abstract

The Ganges-Brahmaputra-Meghna delta is vulnerable to sea level rise from global warming. Based on sea level rise predictions for the year 2100 given in the 6th Assessment Report by the Intergovernmental Panel on Climate Change (IPCC), we examine the effect of uncertainty in sea level rise on maximum tidal elevation statistics at several locations along the Bangladesh coastline using a discretized derived distribution approach. For five IPCC scenarios, the standard deviation in maximum tidal elevation including sea level rise is predicted to increase by between 3% and 61% at three different locations for a 41% increase in the standard deviation of mean sea level rise. By excluding the linear effect of sea level rise, the increase in the standard deviation of maximum tidal elevation is found to vary spatially from 2% to 68% with a 41% increase in the standard deviation of sea level rise.

1. Introduction

Bangladesh is one of the countries most threatened by climate change impact. It is conjectured that oceanic water will penetrate the river system of Bangladesh as the mean sea level rises, and the resulting salt intrusion will adversely affect freshwater resources and food production (Kusche et al., 2016). The rising sea level is also expected to affect the flow-sediment regime, which in turn will alter flood inundation patterns and local sediment balances (Akter et al., 2016). The risen sea level will increase drainage blocking and cause more frequent storm surge inundation (Karim and Mimura, 2008). Sea level rise could even threaten the sustainability of mangrove forests, coral reefs, and salt marshes (Lovelock et al., 2015). It has been suggested that the Sundarbans mangrove forest may be unable to provide a suitable habitat for Bengal tigers after 2070 (Mukul et al., 2019). More than 2 million people residing in

the southern half of Bangladesh are vulnerable to displacement due to sea level rise (Davies et al., 2018). The risks of flooding, salinization, and erosion are expected to increase by the year 2100 in low-lying countries, if proper measures are not adopted (Openheimer et al., 2019). The Bangladesh coast is subsiding, and taken together with sea level rise, the magnitude and frequency of flood events are projected to increase (Ranasinghe et al., 2021; Becker et al., 2020). Consequently, the whole of South Asia is under threat of severe shoreline retreat (Ranasinghe et al., 2021).

Without protective measures, flood inundation risk is likely to increase for densely populated coastal cities in South Asia under the projected sea level rise by 2100, and the impacts of frequent flood events will be severely exacerbated by sea level rise (Yin et al., 2020). Low-lying coastal regions, subject to frequent tropical cyclones, are already under threat of flooding even under low-probability flood events (Yin et al., 2021). Recent research advances in coastal flood risk assessment and prediction include the application of data analytics such as machine learning to estimate actual risk (see e.g., Pollard et al. 2018, Park and Lee, 2020), coastal hydro-morphodynamic process-based models to predict flood inundation (see e.g., Roelvink and Reniers, 2011), dynamic reduced complexity models (see e.g., Purvis et al. 2008; Ramirez et al. 2016, Vousdoukas et al. 2016), and composite vulnerability indices to indicate relative risk (see e.g., Pantusa et al. 2018, and Sahana and Sajjad 2019). Ongoing work is addressing future coastal risk in the context of climate change by considering sea level rise, extreme precipitation, and typhoon events using probabilistic approaches such as multivariate elliptical copulas (Wahl et al. 2016) and Monte Carlo simulations (Vousdoukas et al. 2018), and integrated climatological-hydrodynamic methods (Yin et al. 2020). A recent study by Xu et al. (2022) used an index-based framework to assess the flood risk posed by future sea level rise scenarios in the coastal zone of China. Taken overall, the present research trend is towards the inclusion of climate change impacts in the spatial assessment of coastal flood risk, utilising developments in data analytics and statistical analysis. The present paper complements this trend by proposing a fast method for estimating the propagation of uncertainty in the context of coastal flood risk assessment.

The coastal zone of Bangladesh is densely populated. Its coastline is 710 km long, with coastal and island communities comprising about 38.5 million people, nearly one-third of the total population of Bangladesh (Bangladesh Planning Commission, 2018).

The coastal population of Bangladesh is very vulnerable to natural disasters. Seven major risks have been reported for the coastal zone in a baseline study conducted by the Bangladesh Planning Commission for the Delta Plan 2100 – coastal floods, cyclone and storm surges, riverbank erosion and vulnerability of islands, sea level rise, salinity intrusion, waterlogging, and coastal erosion (Bangladesh Planning Commission, 2018). Furthermore, land scarcity exposes the coastal community to a much higher level of risk, and so policymakers are striving to develop an efficient coastal zone management plan. Formulation of the Bangladesh Delta Plan 2100 commenced in 2014 to establish a long-term holistic and integrated strategy for the delta. The Bangladesh Government's policy is to integrate climate change adaptation with a knowledge-based approach in order to make efficient use of the limited natural resources in Bangladesh. Our research finds that there is considerable uncertainty in maximum tidal elevations due to uncertainty in mean sea level rise. This is particularly important for flood risk assessment and could inform flood mitigation planning in Bangladesh.

Over the recent past, the global mean sea level (GMSL) rise has accelerated for anthropogenic reasons (Becker et al., 2020; Openheimer et al., 2019). Analysis of data from the northern Indian Ocean obtained over a period of more than 40 years up to 2004 has shown the local rate of sea level rise off the Indian sub-continent during that period was 1.06-1.75 mm/year (Brammer, 2014). In its 5th Assessment Report (AR5), the IPCC examined glaciers, ice sheet surface mass balance, ice sheet dynamics, groundwater and reservoirs, gravity and solid Earth effects, thermal expansion, density, and circulation changes, waves and storm surges to forecast sea level change scenarios (Church et al., 2013). The IPCC considered four Representative Concentration Pathway (RCP) scenarios, namely RCP2.6, RCP4.5, RCP6.0, and RCP8.5, based on combinations of contributory factors that had different value ranges. The IPCC predicted 0.44 m, 0.53 m, 0.56 m, and 0.73 m mean rises in global sea level and estimated likely 5-95 percentile ranges for these scenarios (Church et al., 2013).

In the IPCC Special Report on the Ocean and Cryosphere in a Changing Climate (SROCC), the Antarctic contribution to global mean sea level rise was updated due to the availability of new studies since the AR5 report (Openheimer et al., 2019). The RCP scenarios were re-derived with updated mean values and likely ranges. The IPCC's SROCC report predicted sea level rises of 0.43 m (0.29-0.59 m), 0.55 m (0.39-

0.72 m) and 0.84 m (0.61-1.10 m) for the RCP2.6, RCP 4.5 and RCP8.5 scenarios. The Antarctic contribution produced the largest uncertainty in the RCP8.5 scenario. The components underpinning probabilistic sea level rise projections led to different uncertainty ranges, because of variations in methodology, interpretation of findings and definition of uncertainty range among the studies on which SROCC was based. Although the uncertainties projected in the SROCC report are slightly higher than in AR5, the results are generally consistent (Openheimer et al., 2019).

Both the AR5 and SROCC reports utilised a baseline period of 1986-2005, whereas the latest 6th Assessment Report (AR6) by IPCC considered an updated baseline period of 1995-2014 (Fox-Kemper et al., 2021). The AR6 report analysed five carbon emission scenarios, called Shared Socio-economic Pathways (SSPs), to predict sea level rise due to anthropogenic drivers of climate change. The SSP5-8.5, SSP3-7.0, and SSP2-4.5 scenarios represent very high, high, moderate and current levels until mid-century of greenhouse gas (GHG) emissions. The SSP1-1.9 and SSP1-2.6 scenarios represent very low and low GHG emissions which decline to net zero around 2050 followed by net negative emissions (Fox-Kemper et al., 2021). Table 1 lists the median values and 5-95 percentile ranges for these five scenarios.

In this paper, we consider all five SSP scenarios in the IPCC 6th Assessment Report to analyse how uncertainty in sea level rise influences uncertainty in maximum tidal elevation at Tiger Point, Char Purulia, and Sandwip, in the Meghna estuary, Bangladesh. It should be noted that none of the IPCC reports considered land subsidence in projections of GMSL because of the high dependence on local conditions (Fox-Kemper et al., 2021; Oppenheimer et al., 2019; Church et al., 2013).

Under the aegis of the Bangladesh Water Development Board (https://www.bwdb.gov.bd/project), extensive embankment construction has been undertaken along the Bangladesh coastline (including the three locations of interest). These embankments have been designed to protect people and properties in nearby cities and villages from flood inundation and land erosion. Given an accurate estimate of the uncertainty in maximum tidal elevation arising from uncertainty in mean sea level rise, then the resulting effect on risk can be assessed properly, and safety factors modified if necessary during the embankment design phase. Furthermore, flood

mitigation planning measures and warning system operations can be executed more effectively by taking such uncertainty into consideration.

Bangladesh is extremely poor in terms of field data, and very often it becomes difficult to establish a validated hydrodynamic model. Uncertainty analysis, therefore, offers a suitable approach for parameter studies in this region. Noting that the IPCC prediction itself contains uncertainty in mean sea level rise, the method presented herein is very efficient at estimating the propagation of uncertainty from mean sea level rise to maximum tidal elevation. (A brief comparison between different uncertainty propagation methods is given in Section 1 of the Supplementary Information.) Sea level rise is likely to promote many natural and societal disasters, such as salinity intrusion, storm surge inundation, land loss, displacement and migration of people, reduced food and water security, lower biodiversity, and ecological damage. The research approach presented herein is particularly appropriate to the assessment of multiple coastal risks.

For about fifty years, an analytic version of the derived distribution approach has been applied to problems involving parameter uncertainty, where the functional dependence of the output parameter on the input parameter is known. Ang and Tang (1975) demonstrated that the approach directly mapped the probability density function of an uncertain input parameter onto that of an output parameter. By relating uncertainty to the variation of the input parameter about its mean value, it is then possible to estimate the propagated uncertainty from the variation of the output parameter. The method extends to all higher moment statistics, such as skewness, and kurtosis, and so provides a very useful way of examining the overall effect of parameter uncertainty on the system. The analytical version of the derived distribution method has been widely applied by hydrologists and water resources engineers, e.g., for flood frequency estimation (Loukas, 2002), flood prediction in a poorly gauged basin in Italy (Brocchiola and Rosso, 2009), stormwater quality modelling (Chen and Adams, 2007), and variability in annual precipitation (Meier et al., 2016). A discrete approach was adopted by Kreitmair et al. (2019) to estimate uncertainty propagation in tidal stream power assessment. Sarwar and Borthwick (2023) adopted the discrete approach to estimate uncertainty in the deposition rate of suspended cohesive sediment. To the authors' knowledge, our paper is the first to report on the application of the numerical

analogue of the derived distribution approach to maximum tidal elevations in the context of an actual large-scale bay subject to sea level rise. A basic hydrodynamic model has been established for this study using the freely available open access modeling tool Delft3D. With further development of this model, the same method can be applied to risk assessments related to flood inundation, sea level rise, land erosion and accretion, salinity intrusion, cyclonic surges, and ocean wave propagation, etc., contributing in the future to the planning and management of the coastal zone of Bangladesh.

2. Methods

Figure 1 shows the study area, computational domain, and three locations of interest. The input bathymetry (Figure 2) comprised measured bed elevations of rivers (data obtained from MorphoFlood project, IHE Delft, The Netherlands) and land elevations of islands (downloaded from the Earthexplorer website of the United States Geological Survey (USGS); https://earthexplorer.usgs.gov/). The computational model followed the local projected co-ordinate system Bangladesh Transverse Mercator (BTM). This is because Bangladesh falls under two UTM zones: 45N and 46N, and so the local co-ordinate system BTM is used in Bangladesh to avoid the complication of having two UTM zones. Land elevation data (SRTM data) were downloaded from Earthexplorer webpage (https://earthexplorer.usgs.gov/) belonging to the United States Geological Survey (USGS). The resulting data were available in WGS 1984 geographic co-ordinate system in longitude and latitude form and were converted to BTM before incorporation in the model. Output maps were produced in geographic co-ordinate system WGS 1984 (see e.g., Figure 1 and Figure 2) for universal communication.

It should be noted that a high-accuracy map for global terrain elevation called Multi-Error-Removed Improved-Terrain DEM (MERIT DEM) has recently become available (http://hydro.iis.u-tokyo.ac.jp/~yamadai/MERIT_DEM/). MERIT DEM separates out certain major error components in the SRTM DEM and AW3D DEM including speckle noise, stripe noise, absolute bias, and tree height bias (Yamazaki et al., 2017). Speckle (or multiplicative) noise refers to the random error generated through variation in surface reflectance over a few pixels. Stripe noise is a regular, 500 m to 1 km, variation in elevation caused by residual mast motion error for SRTM data and artificial

tilt in elevation for AW3D DEM (Yamazaki et al., 2017). Absolute bias is a shift in average elevation over large areas, whose linear dimension usually exceeds 20 km. Tree height bias arises from instrumentation errors in measuring ground elevation beneath the tree canopy. However, such errors are predominantly terrestrial and so have only a minimal effect on the hydrodynamic model used herein because the model mostly comprises sea and river areas where bathymetric field data were utilized. Land elevation data were required for a few islands near the coast to facilitate wetting and drying in the hydrodynamic simulation. Apart from the coastline, most of the land areas of these islands remained dry throughout all the simulations, and so the land elevation data did not influence the coastal flow patterns considered herein. Moreover, Bhola, the largest island, has an area of 1441 km^2, length 130 km, width 25 km, and highest elevation 1.8 m above mean sea level. Other islands are even smaller. Thus, the islands do not cover a significantly large area compared to the whole domain which occupies several hundred km^2.

The depth-averaged version of Delft3D-FLOW software (Deltares, 2600 MH Delft, The Netherlands, https://oss.deltares.nl/web/delft3d) was used to simulate the flow hydrodynamics in the Meghna estuary and hence to predict the maximum tidal elevation (resulting from river flow and tide). The cell dimension of the curvilinear grid varied from 100 m in the estuary to 3400 m in the bay. Smaller cell size was provided near the location of interest to reproduce the bathymetry and channel alignment correctly, and hence minimize computational error. Larger cell size was provided in the bay far from the estuary, where the bathymetry is less complex. The grid followed the riverbank and coastline as closely as possible, but the fractal geometry along the coast comprising multiple tributaries was obviously simplified. The computational grid covered the entire bay, including islands and tidal flats to facilitate unconstrained wetting and drying. The Delft3D model contained two upstream open boundaries carrying river discharge and one downstream open boundary with tidal constituents. For simplification purposes, constant river discharge values were prescribed at both upstream boundaries. Flow inputs for the Padma river (located beyond the confluence between the Ganges and Brahmaputra) and the Meghna river were set to 120,000 m^3/s and 20,000 m^3/s respectively (Figure 3). These river discharges represented the annual peak flood in the year 2007. The bathymetry used in the model corresponded to the year 2007-2008 (Figure 3), and so river discharges for the same time period

were input to the model. Both sets of river data were obtained with permission from the MorphoFlood project by IHE Delft, The Netherlands. At the downstream boundary, the flow input comprised M_2 and S_2 tidal components, which are dominant in the Bay of Bengal. Table 2 lists the tidal components at the east and west ends of the offshore boundary. It also lists the representative amplitudes and phases, obtained from the TPXO 8.0 database using the DelftDashboard tool (https://publicwiki.deltares.nl/display/DDB/Delft+Dashboard) from Deltares, The Netherlands. Further details of the model are given by Sarwar (2021).

Bed friction was incorporated using the Manning's roughness parameter, *n*. In absence of field data concerning bed roughness, we adopted the approach proposed by Soulsby (1997) and Whitehouse et al. (2000) to determine the spatial distribution of Manning's *n* as follows. Using values of depth-averaged velocity $\bar{u}$ and water depth *h* obtained from the Delft3D model, the log-law was invoked to determine the bed friction velocity iteratively from

$$u_* = \frac{\kappa \bar{u}}{\left(ln\frac{h}{z_0} - 1\right)} \tag{1}$$

where κ is the von Kármán constant (~0.4), *h* is water depth, and z_0 is the bed roughness length given by

$$z_0 = \frac{k_s}{30}\left[1 - \exp\left(\frac{-u_* k_s}{27\nu}\right)\right] + \frac{\nu}{9u_*} \quad , \tag{2}$$

in which k_s = 2.5d_{50} is the Nikuradse roughness, d_{50} is the median particle diameter, and ν is the kinematic viscosity of water. Assuming that the dominant contribution was from skin friction, the bed roughness drag coefficient C_D was then estimated from

$$C_D = \left[\frac{\kappa}{\ln\frac{h}{z_0} - 1}\right]^2 \quad . \tag{3}$$

The Manning bed roughness coefficient was finally determined (assuming the ocean was analogous to a very wide channel from the perspective of hydraulic radius) from:

$$n = \sqrt{C_D \frac{h^{1/3}}{g}}, \tag{4}$$

where *g* is acceleration due to gravity. Figure 3 displays the resulting contour map of Manning's *n* whose value lies roughly in the range 0.01-0.03 s/m$^{1/3}$ for the Meghna estuary under conditions of zero sea level rise.

The Delft3D model was then run for different values of sea level rise varying from 0.1 m to 1.2 m. After a spin-up of 5 days, the model was run for a further 2 spring-neap cycles, and predicted maximum tidal elevations were recorded at the three locations of interest. Functional relationships were then established between sea level rise and maximum tidal elevation at the three locations of interest (marked on Figure 1). Truncated normal distributions of sea level rise were fitted to 2100 data for IPCC global scenarios SSP1-1.9, SSP1-2.6, SSP2-4.5, SSP3-7.0 and SSP5-8.5. Convergence tests were carried out to decide the number of bins required for accurate discretization of the probability distribution of sea level rise (see Section 1 of Supplementary Information). The probability distribution for sea level rise was obtained using the mean value and the 90% confidence limit listed by IPCC for each scenario (Fox-Kemper et al., 2021).

Then the numerical derived distribution approach (originally proposed for uncertain tidal stream power assessment by Kreitmair et al., 2019) was adopted to derive the probability distribution of maximum sea level rise. In the numerical derived distribution method, probability distributions of independent and dependent variables are considered in discrete, rather than continuous, form. The derived distribution approach is summarized as follows. First, an analytical expression is specified for the probability density function of the input parameter, with the variance representing uncertainty. Then, the cumulative distribution function of the input parameter is determined by integration, and the cumulative distribution function of the output parameter is then evaluated through conservation of probability noting the functional relationship between the input and output. Being direct, the derived distribution method offers fast assessment of uncertainty propagation provided the functional relationship between input and output is monotonic. The derived distribution approach is based on the concept of conservation of probability (Benjamin and Cornell, 1970). A full description is given by Sarwar (2021). In short, after changing the variable of integration, the resulting cumulative distribution function of the output variable is differentiated to provide its probability density function.

Let the Manning roughness coefficient *n* be a random variable represented by a Gaussian distribution with mean μ_n and standard deviation σ_n. Then, the probability that the value of n lies between n_A and n_B, where $n_A < n_B$, may be written

$$\Pr(n_A < n < n_B) = \int_{n_A}^{n_B} N(n|\,\mu_n, \sigma_n^2)\,\mathrm{d}n$$

$$= \Phi(n_B) - \Phi(n_A)$$

$$= \frac{1}{2}\left[\mathrm{erf}\left(\frac{n_B-\mu_n}{\sigma_n\sqrt{2}}\right) - \mathrm{erf}\left(\frac{n_A-\mu_n}{\sigma_n\sqrt{2}}\right)\right] . \qquad (5)$$

For finely spaced discrete values of n, then the likelihood of a particular value n_i is given by

$$\Pr(n = n_i) = \Pr\left(n_{i-\frac{1}{2}} \le n < n_{i+\frac{1}{2}}\right)$$

$$= \Pr\left(\frac{1}{2}\left(n_{i-\frac{1}{2}} + n_i\right) \le n < \frac{1}{2}\left(n_i + n_{i+\frac{1}{2}}\right)\right)$$

$$= \frac{1}{2}\left[\mathrm{erf}\left(\frac{n_{i+\frac{1}{2}}-\mu_n}{\sigma_n\sqrt{2}}\right) - \mathrm{erf}\left(\frac{n_{i-\frac{1}{2}}-\mu_n}{\sigma_n\sqrt{2}}\right)\right] . \qquad (6)$$

From the definition of the derived probability distribution, equation (6) relates to the probability of maximum tidal elevation Z, given that $Z = f(n)$. Hence, the expected value and variance of Z may be determined as

$$E[Z] = \sum_i Z_i(n = n_i)\Pr(n = n_i) \quad , \qquad (7)$$

and

$$\sigma_Z^2 = \sum_i (Z_i(n = n_i) - E[Z])^2 \Pr(n = n_i) \, , \qquad (8)$$

with (higher) m^{th} order statistical moments given by

$$\mu_m = \sum_i (Z_i(n = n_i) - E[Z])^m \Pr(n = n_i) \, . \qquad (9)$$

Here $m = 3$ denotes skewness (i.e., asymmetry) and $m = 4$ denotes kurtosis (i.e., tailed-ness or peakedness).

The detailed procedure is as follows:

i. Carry out numerical simulations and tabulate results for input parameter x against output parameter *y*. Use a cubic spline to obtain interpolated values. Plot *y* against x.

ii. Select mean μ_x and standard deviation σ_x of the input parameter data.

iii. Select a standard probability distribution (e.g. normal distribution) and plot:

- Probability density function, PDF $p(x)$
- Cumulative density function, CDF $c(x)$.

iv. Check the results by calculating the expected value $E[x]{\sim}x$ and variance, $Var[x]{\sim}\sigma_x^2$.

v. Divide the PDF and CDF into a prescribed number i_{max} of bins, ensuring that the probabilities are always positive-valued.

vi. For each bin from $i = 1,2\ldots, i_{max}$ determine the middle value x_i. Use the relationship between *y* and x to determine corresponding y_i

vii. Determine CDF values $c(x)_{i-1/2}$ and $c(x)_{i+1/2}$ at either end of the bin, and hence determine the probability $Pr_i = c(x)_{i+1/2} - c(x)_{i-1/2}$.

viii. Calculate expected value of the output parameter from $E[y] = \sum_{i=1}^{i_{max}} Pr_i\, y_i$.

ix. Calculate variance in output parameter from $Var[y] = \sum_{i=1}^{i_{max}} Pr_i (y_i - E[y])^2$.

x. Calculate skewness from $Skew[y] = \sum_{i=1}^{i_{max}} Pr_i (y_i - E[y])^3$.

xi. Calculate kurtosis from $Kurt[y] = \sum_{i=1}^{i_{max}} Pr_i (y_i - E[y])^4$

xii. Determine output values at either end of each bin, $y_{i-1/2}$ and $y_{i+1/2}$, for $c(x)_{i-1/2}$ and $c(x)_{i+1/2}$ using the relationship between y and x. Hence determine bin widths, $\Delta y_i = y_{i+1/2} - y_{i-1/2}$.

xiii. Determine PDF for y as $p(y)_i = \frac{Pr_i}{\Delta y_i}$ and plot $p(y)_i$ against y_i for $i = 1,2\ldots, i_{max}$ (Figure S3).

xiv. Hence determine CDF of y by numerical integration, $c(y)_i = \sum_{i=1}^{i_{max}} p(y)_i \Delta y_i$, and plot $c(y)_i$ against y_i for $i = 1,2\ldots, i_{max}$. Whereas the bin widths Δx_i may each have the same value, the bin widths Δy_i will be different to each other if there is a non-linear relationship between y and x.

Figure 4 presents a graphical representation of the probability transfer process.

3. Uncertainty Analysis

Figure 5 shows the functional relationship between sea level rise and maximum tidal elevation (including the rise in sea level from datum), probability distribution (PDF) of maximum tidal elevation and cumulative probability distribution (CDF) of maximum tidal elevation derived from the PDF of sea level rise using the numerical derived distribution approach at Sandwip, Tiger Point, and Char Purulia along the coastline of Bangladesh. Table 3 lists the expected values and higher order moments for maximum tidal elevation obtained for the five scenarios of sea level rise. As the mean sea level rise increases from 0.38 m to 0.77 m (103% increase), the expected maximum tidal elevation at Sandwip increases by about 15%. The standard deviation of maximum tidal elevation at Sandwip increases by 3% for a 41% increase in standard deviation in sea level rise. The non-dimensional skewness remains about zero, indicating the PDFs to be truncated normal distributions for maximum tidal elevation. The magnitude of non-dimensional kurtosis remains very close to 3 in each case, in keeping with a truncated normal distribution. As the mean value of sea level rise increases, the peak in the PDF of maximum tidal elevation at Sandwip progressively moves to higher values of maximum tidal elevation, but the magnitude of the peak decreases. Similarly, the standard deviation of maximum tidal elevation increases as the mean value of sea level rise increases.

At Tiger Point, both the river discharge and tide are dominant forcing parameters. Increasing sea level rise causes a corresponding increase in tidal elevation. As at Sandwip, the peak in the PDF of maximum tidal elevation is reached at progressively higher values of maximum tidal elevation as the sea level rise increases. Again, the magnitude of the peak of the PDF of maximum tidal elevation decreases with increasing sea level rise. The expected value of maximum tidal elevation increases by about 20% when the mean sea level rise alters from 0.38 m to 0.77 m (103% increase),

and the standard deviation in maximum tidal elevation increases by about 38% as the standard deviation of sea level rise increases by 41% (Table 3). The non-dimensional skewness is almost zero and the non-dimensional kurtosis is about 3, indicating that the five distributions of maximum tidal elevation can be effectively represented by truncated normal distributions.

The third location at which the propagation of uncertainty from sea level rise to maximum tidal elevation is considered is at Char Purulia. It can be seen in Table 3 that the expected value of maximum tidal elevation at Char Purulia increases by about 8% with a 103% increase in the mean value of sea level rise. The standard deviation in maximum tidal elevation increases by about 61% for a 41% increase in the standard deviation in sea level rise. The magnitude of non-dimensional skewness for all the PDFs is invariably very small, indicating that the probability density function of maximum tidal elevation is close to a normal distribution. The non-dimensional kurtosis has values near 3 which again indicate the PDF is very well represented by a normal distribution.

At all three locations, the non-dimensional kurtosis remained at a value of about 3, indicating that the probability distributions are truncated normal distributions. There is no specific increasing or decreasing trend in the non-dimensional kurtosis (Table 3), but instead there is a decrease in the trend in peakedness of the probability distribution (Figure 5). By definition, non-dimensional kurtosis expresses how far the extreme values of the distribution are dispersed from the mean (eq. 9, where $m = 4$). The shape of the probability distribution of maximum tidal elevation depends on the probability distribution of sea level rise, and the relationship between maximum tidal elevation and sea level rise. The PDFs of sea level rise have more dispersed extreme values when the sea level rise increases. Since maximum tidal elevation is proportional to sea level rise (Figure 5, row 1), the probability distributions of maximum tidal elevation also contain more dispersed extreme values with a lower peak.

The foregoing results quantify how uncertainty differs from place to place in the vicinity of the Bangladesh coast. It is expected that the maximum tidal elevation will increase with the rise of sea level; however, for the same global mean sea level rise (same uncertainty and same PDF), it is found that the values of uncertainty in maximum tidal elevations at different locations differ from each other. The geometry of the bottom

surface plays a vital role causing tidal asymmetry. Char Purulia experiences additional effects from river discharge and channel curvature on its flow regime. So, the relationships between sea level rise and maximum tidal elevation vary, and that causes the PDFs and uncertainty to change across the locations considered.

Next, the rise in sea level is subtracted from the model output of maximum tidal elevation (denoted by s from here on); this enables assessment as to how uncertainty in sea level rise affects uncertainty in maximum tidal elevation when the linear effect of sea level rise is removed. Figure 6 shows the cubic spline relationship between s at Sandwip, Char Purlia, and Tiger Point, as well as the derived probability distribution of s. In this case, the functional relationships are no longer linear, although the functions are either monotonically increasing or decreasing.

Table 3 summarizes the expected values and statistical moments of s at the three selected locations. As the mean of sea level rise increases 103% at Sandwip, the expected s increases by only 2%, but the standard deviation increases by 68%. The non-dimensional skewness confirms that the distribution related to SSP1-19 sea level rise is left-skewed (non-dimensional skewness is negative). The probability density distribution is almost a normal distribution for SSP1-1.26 (near-zero non-dimensional skewness). The PDF becomes right-skewed for the SSP2-4.5 scenario (positive non-dimensional skewness). Then the PDFs become left-skewed for SSP3.-7.0 and SSP5-8.5 scenarios (negative non-dimensional skewness). All the respective CDFs reach 1 despite their various shapes. The functional relationship between s and sea level rise is monotonic, but non-linear where the slope changes multiple times. Thus the derived probability distributions of s exhibit starkly different shapes. The non-dimensional kurtosis for SSP1-2.6 is well above 3, which indicates that the shape of distribution is narrower than a standard normal distribution, whereas for SSP3-7.0 the distribution is lower than 3, indicating that the probability distribution is flatter than a normal distribution. For the other three distributions, the non-dimensional kurtosis is slightly above 3, suggesting that these are slightly narrower than a normal distribution.

At Tiger Point, as the sea level rise increases, there is a monotonic decreasing trend in s and the function is not linear. From Table 3, all the PDFs of s have non-dimensional kurtosis of about 3, which indicates that the steepness of these PDFs is very close to

that of the standard normal distribution. The non-dimensional skewness values for SSP1-1.9 and SSP1-2.6 are positive, so the distributions are right-skewed. The other three PDFs have negative non-dimensional skewness, and so are left-skewed. The mean of s hardly varies (with 1% reduction) indicating it is almost insensitive to sea level rise. However, the standard deviation increases by about 54%, indicating that there is much higher propagation of uncertainty.

Derived probability distributions for s at Char Purulia are shown in the third column of panels in Figure 6, where it can be seen that the tallest peak in the PDF occurs for SSP5-8.5. The PDFs and CDFs are similar across the scenarios in that they all exhibit near-normal distributions. Table 3 lists the expected values and other statistical parameters. The non-dimensional skewness shows that the three probability distributions are slightly skewed to the right of the mean of the distribution (positive values), and the non-dimensional kurtosis (all values near 3) suggests that the derived PDFs are very close in form to a standard normal distribution. When the mean of the sea level rise increases by 103%, the mean of s decreases by about 3% only. An increase of 41% in standard deviation in sea level rise leads to an almost invariable standard deviation (2% variation) in s.

The functional relationship between sea level rise and s indicates that the effect of global mean sea level rise on the regional sea level rise near the coast of Bangladesh is not a straightforward phenomenon. When a tide enters shallow water, it is deformed. The regional sea level rise varies spatially, and may not be equal to the amount of global sea level rise. Thus, when the global sea level rise is deducted from the local maximum tidal elevation, the remaining water level can exhibit either increasing or decreasing trends. The expected value of s does not significantly vary in space, unlike the standard deviation which varies across the three locations (from 2% variation at Char Purulia to 68% at Sandwip). The primary reason for this large span of standard deviation concerns the local bed topography, and the resulting hydrodynamics. More specifically, the fractal geometry of the land, the narrow gorges containing river channels, shallow mudflats at the mouth of the estuary, amplification of the flood tide as it crosses the continental shelf when entering the estuary and passing over mudflats and through islands, all cause a striking variation in flow pattern at different locations.

In future work, it is hoped that a clearer picture will emerge by considering more locations along the coast and creating locally fine maps of key statistics such as *s*.

Lastly, in order to examine the effect of mean sea level rise on excess maximum tidal elevation, further analysis is carried out concerning the statistical relationship between excess maximum tidal elevation and sea level rise. Here, the excess maximum tidal elevation is defined as the maximum tidal elevation minus both the mean sea level rise and the reference maximum tidal elevation obtained for no sea level rise. Figure 7 shows the cubic spline fit to data on excess maximum tidal elevation at Sandwip, Tiger Point, and Char Purulia plotted against sea level rise. The relationship at Sandwip is nonlinear, even though there is a progressive increase in excess maximum tidal elevation from about 0.02 m to 0.12 m for a sea level rise from 0.1 to 1.2 m. All the PDFs and functional relationships shown in Figure 7 show the same trend in PDFs and functional relationship as in Figure 6 (i.e., cases of maximum tidal elevation minus sea level rise). Table 3 lists the expected value of excess maximum tidal elevation and other statistical moments. When the mean of the sea level rise increases by 103%, the expected value of excess maximum tidal elevation at Sandwip increases by 85%, at Tiger Point decreases by 92%, and at Char Purulia decreases by 76%. With an increase in standard deviation in sea level rise of 41%, the standard deviation in excess maximum tidal elevation at Sandwip increases by 68%, at Tiger Point decreases by 54%, and at Char Purulia decreases by 2%.

A more detailed description of the uncertainty analysis is provided by Sarwar (2021), and its extension to sediment transport and bed morphological change by Sarwar and Borthwick (2023).

4. Conclusions

This article has investigated the effect of sea level rise on maximum tidal elevation at three locations along the Bangladesh coastline, based on fits of IPCC 6th Assessment scenario forecasts (Fox-Kemper et al., 2021) of sea level rise by 2100 to a truncated normal probability density distribution. For the five different IPCC scenarios considered, the standard deviation (i.e., uncertainty) in maximum tidal elevation including sea level rise increased by between 3% at Sandwip and 61% at Char Purulia for a 41% increase in standard deviation of mean sea level rise. By excluding the linear

effect of sea level rise, the increase in standard deviation in maximum tidal elevation was found to vary remarkably from 2% at Char Purulia to 68% at Sandwip for the 41% increase in standard deviation of sea level rise. For the cases considered, a novel numerical analogy of the derived distribution method proved effective at estimating output uncertainty in maximum tidal elevation using results from very few model simulations.

Mean and extreme sea level rise promote coastal hazards that include permanent submergence of land, more frequent intense flooding, severe coastal erosion, drainage congestion, salinization of soil, groundwater and surface water, and ecosystem degradation (Openheimer et al., 2019). Bangladesh is a low-lying country, and its coastal communities are under substantial risk of such coastal hazards. The IPCC SROCC report (Openheimer et al., 2019) suggested that century-scale adaptation and protection strategy is needed for low-lying countries, given that their communities may experience the upper end of the high to very-high risk scenarios. Despite the large uncertainty, adaptation planning and implementation for 2100 can be beneficial. Decision-analysis methods, particularly for situations with large uncertainty are available nowadays and can be used to assist decisions covering timescales from decades to centuries. Thus, the present study of uncertainty in maximum tidal elevation is of high importance for coastal regions prone to inundation, and specifically relevant to coastal management strategies in Bangladesh.

Although only three locations were chosen for quantification of output uncertainty arising from a single input parameter (i.e., sea level rise), the present analysis is straightforward to extend to the estimation of output uncertainty for multiple input parameters at multiple locations along the coastline of Bangladesh. Such an approach, enhanced by bias correction, would provide a holistic picture of uncertainty propagation throughout the whole coastal region of Bangladesh, contributing to the planning and management of the coastal zone of Bangladesh for many years to come.

Data Availability

Data sources for land elevation, bed level, tidal constituents, river discharge and sea level rise are available within the Main Text and Supplementary Information.

Supplementary Information is available with the online version of this paper.

Acknowledgements

The first author is grateful to the Schlumberger Foundation Faculty for the Future Fellowship program for its financial support.

Author Contributions

A.G.L.B. and S.S. designed the research. S.S. established the model and performed the research. S.S. and A.G.L.B. wrote the paper and contributed to interpretation of the findings.

Competing interests statement

The authors declare no competing interests.

References

Akter, J., Sarker, M.H., Popescu, I. & Roelvink, D. (2016). Evolution of the Bengal Delta and its prevailing processes. *Journal of Coastal Research, 32,* 1212–1226.

Ang, A.H-S. & Tang, W.H. (1975). *Probability concepts in engineering planning and design, vol. 1: Basic principles.* John Wiley and Sons, Inc.

Bangladesh Planning Commission (2018). *Bangladesh Delta Plan 2100 Baseline Studies: Volume 1 - Water Resource Management*. General economic Division, Bangladesh Planning Commission, Government of People's Republic of Bangladesh.

Becker, M., Papa, F., Karpytchev, M., Delebecque, C., Krien, Y., Khan, J.U., Ballu, V., Durand, F., Cozannet, G.L., Islam, A.K.M.S., Calmant, S. & Shum, C.K. (2020). Water level changes, subsidence, and sea level rise in the Ganges–Brahmaputra–Meghna delta. *Proceedings of the National Academy of Sciences of the United States of America, 117,* 1867-1876.

Benjamin, J.R. & Cornell, C.A. (1970). *Probability, Statistics, and Decision for Civil Engineers*. McGraw-Hill.

Brammer, H. (2014). Bangladesh's dynamic coastal regions and sea-level rise. C*limate Risk Management, 1,* 51–62.

Brocchiola, D. & Rosso, R. (2009). Use of a derived distribution approach for flood prediction in poorly gauged basins: A case study in Italy. *Advances in Water Resources, 32,* 1284-1296.

Chen, J. & Adams, B.J. (2007). A derived probability distribution approach to stormwater quality modelling. *Advances in Water Resources, 30,* 80-100.

Church, J.A., P.U. Clark, A. Cazenave, J.M. Gregory, S. Jevrejeva, A. Levermann, M.A. Merrifield, G.A. Milne, R.S. Nerem, P.D. Nunn, A.J. Payne, W.T. Pfeffer, D. Stammer & A.S. Unnikrishnan, (2013). Sea Level Change. In Stocker, T.F., D. Qin, G.-K. Plattner, M. Tignor, S.K. Allen, J. Boschung, A. Nauels, Y. Xia, V. Bex & P.M. Midgley (Eds), *Climate Change 2013: The Physical Science Basis. Contribution of Working Group I to the Fifth Assessment Report of the Intergovernmental Panel on Climate Change.* Cambridge University Press.

Davies, K.F., Bhattachan, A., D'Odorico, P. & Suweis, S. (2018). A universal model for predicting human migration under climate change: examining future sea level rise in Bangladesh. *Environmental Research Letters, 13,* 064030.

Fox-Kemper, B., H.T. Hewitt, C. Xiao, G. Aðalgeirsdóttir, S.S. Drijfhout, T.L. Edwards, N.R. Golledge, M. Hemer, R.E. Kopp, G. Krinner, A. Mix, D. Notz, S. Nowicki, I.S. Nurhati, L. Ruiz, J.-B. Sallée, A.B.A. Slangen, & Y. Yu, (2021). Ocean, Cryosphere and Sea Level Change. In Masson-Delmotte, V., P. Zhai, A. Pirani, S.L. Connors, C. Péan, S. Berger, N. Caud, Y. Chen, L. Goldfarb, M.I. Gomis, M. Huang, K. Leitzell, E. Lonnoy, J.B.R. Matthews, T.K. Maycock, T. Waterfield, O. Yelekçi, R. Yu, & B. Zhou (Eds.), *Climate Change 2021: The Physical Science Basis. Contribution of Working Group I to the Sixth Assessment Report of the Intergovernmental Panel on Climate Change* (pp. 1211–1362). Cambridge University Press. doi:10.1017/9781009157896.011.

Karim, M. & Mimura, N. (2008). Impacts of climate change and sea-level rise on cyclonic storm surge floods in Bangladesh. *Global Environmental Change, 18,* 490-500.

Kreitmair, M.J., Draper, S., Borthwick, A.G.L. & van den Bremer, T.S. (2019). The effect of uncertain bottom friction on estimates of tidal current power. *Royal Society Open Science, 6,* 180941.

Kusche, J., Uebbing, B., Rietbroek, R., Shum, C.K. & Khan, Z.H. (2016). Sea level budget in the Bay of Bengal (2002-2014) from GRACE and altimetry. *Journal of Geophysical Research: Oceans, 121,* 1194-1217.

Loukas, A. (2002). Flood frequency estimation by a derived distribution procedure. *Journal of Hydrology, 255,* 69-89.

Lovelock, C.E., Cahoon, D.R., Friess, D.A., Guntenspergen, G.R., Krauss, K.W., Reef, R., Rogers, K., Saunders, M.L., Sidik, F., Swales, A., Saintilan, N., Thuyen, L.X. & Triet, T. (2015). Vulnerability of Indo-Pacific mangrove forests to sea-level rise. *Nature, 526,* 559-563.

Meier, C.I., Moraga, J.S., Pranzini, G. & Molnar, P. (2016). Describing the interannual variability of precipitation with the derived distribution approach: effects of record length and resolution. *Hydrology and Earth System Sciences, 20,* 4177-4190.

Mukul S.A., Alamgir, M., Sohel, M.S.I., Petina L. Pert, P.L., Herbohn, J., Turton, S.M., Khan, M.S.I., Munim, S.A., Reza,A.H.M.A. & Laurance, W.F. (2019). Combined effects of climate change and sea-level rise project dramatic habitat loss of the globally endangered Bengal tiger in the Bangladesh Sundarbans. *Science of the Total Environment, 663,* 830-840.

Oppenheimer, M., B.C. Glavovic , J. Hinkel, R. van de Wal, A.K. Magnan, A. Abd-Elgawad, R. Cai, M. Cifuentes-Jara, R.M. DeConto, T. Ghosh, J. Hay, F. Isla, B. Marzeion, B. Meyssignac, & Z. Sebesvari (2019). Sea Level Rise and Implications for Low-Lying Islands, Coasts and Communities. In H.-O. Pörtner, D.C. Roberts, V. Masson-Delmotte, P. Zhai, M. Tignor, E. Poloczanska, K. Mintenbeck, A. Alegría, M. Nicolai, A. Okem, J. Petzold, B. Rama, N.M. Weyer (Eds.), *IPCC Special Report on the Ocean and Cryosphere in a Changing Climate* (pp. 321–445). Cambridge University Press. doi:10.1017/9781009157964.006

Pantusa, D., D'Alessandro, F., Riefolo, L., Principato, F. & Tomasicchio G.R. (2018) Application of a coastal vulnerability index. A case study along the Apulian Coastline, Italy. *Water*,10: 1–16.

Park, S.-J. & Lee, D.-K. (2020) Prediction of coastal flooding risk under climate change impacts in South Korea using machine learning algorithms. *Environmental Research Letters*, 15(9): 094052, 10 pages.

Pollard, J.A., Spencer, T., & Jude, S. (2018) Big Data Approaches for coastal flood risk assessment and emergency response, *WIREs Climate Change*, 9(5): e543. 14 pages.

Purvis, M.J., Bates, P.D., and Hayes, C.M. (2008) A probabilistic methodology to estimate future coastal flood risk due to sea level rise, *Coastal Engineering*, 55: 1062–1073.

Ramirez, J.A., Lichter, M., Coulthard, T.J., & Skinner, C. (2016) Hyper-resolution mapping of regional storm surge and tide flooding: comparison of static and dynamic models, *Natural Hazards*, 82, 571–590.

Ranasinghe, R., A.C. Ruane, R. Vautard, N. Arnell, E. Coppola, F.A. Cruz, S. Dessai, A.S. Islam, M. Rahimi, D. Ruiz Carrascal, J. Sillmann, M.B. Sylla, C. Tebaldi, W. Wang, & R. Zaaboul, (2021). Climate Change Information for Regional Impact and for Risk Assessment. In Masson-Delmotte, V., P. Zhai, A. Pirani, S.L. Connors, C. Péan, S. Berger, N. Caud, Y. Chen, L. Goldfarb, M.I. Gomis, M. Huang, K. Leitzell, E. Lonnoy, J.B.R. Matthews, T.K. Maycock, T. Waterfield, O. Yelekçi, R. Yu, & B. Zhou (Eds.), *Climate Change 2021: The Physical Science Basis. Contribution of Working Group I to the Sixth Assessment Report of the Intergovernmental Panel on Climate Change* (pp. 1767–1926). Cambridge University Press. doi:10.1017/9781009157896.014

Roelvink, D. & Reniers, A. (2011) *A Guide to Modeling Coastal Morphology*. Advances in Coastal and Ocean Engineering: Volume 12, World Scientific, Singapore. ISBN 978-981-4304-25-2.

Sahana, M. & Sajjad, H. (2019) Vulnerability to storm surge flood using remote sensing and GIS techniques: a study on Sundarban Biosphere Reserve, India. *Remote Sensing Applications: Society and Environment*, 13: 106–120.

Sarwar, S. (2021) *Estimation of uncertainty in the hydro-morphodynamic characteristics of the Meghna Estuary, Bangladesh*. PhD. Thesis, The University of Edinburgh, UK.

Sarwar, S. & Borthwick A.G.L. (2023) Estimate of uncertain cohesive suspended sediment deposition rate from uncertain floc size in Meghna estuary, Bangladesh. *Estuarine, Coastal and Shelf Science, 281.* 15 pages.

Soulsby, R. (1997). *Dynamics of marine sands: A manual for practical applications.* Thomas Telford Publications.

Vousdoukas, M.I., Voukouvalas, E., Mentaschi, L., Dottori, F. & Giardino, A. (2016) Developments in large-scale coastal flood hazard mapping. *Natural Hazards and Earth System Sciences*, 16: 1841–1853.

Vousdoukas, M.I., Mentaschi, L., Voukouvalas, E., Verlaan, M., Jevrejeva, S., Jackson, L.P., & Feyen L. (2018). Global probabilistic projections of extreme sea levels show intensification of coastal flood hazard. *Nature Communications*, 9(1): 1–12.

Wahl, T., Plant, N.G. & Long, J.W. (2016) Probabilistic assessment of erosion and flooding risk in the northern Gulf of Mexico. *Journal of Geophysical Research: Oceans*, 121: 3029–43.

Whitehouse, R., Soulsby, R., Roberts, W. & Mitchener, H. (2000). *Dynamics of estuarine muds: A manual for practical applications.* Thomas Telford Publications.

Xu, H., Hou, X., Li, D., Wang, X., Fan, C., Du, P. & Song, B. (2022) Spatial assessment of coastal flood risk due to sea level rise in China's coastal zone through the 21st century. *Frontiers in Marine Science*, 9: 945901.

Yamazaki, D., Ikeshima, D., Tawatari, R., Yamaguchi, T., O'Loughlin, F., Neal, J.C., Sampson, C.C., Kanae, S. & Bates, P.D. (2017). A high-accuracy map of global terrain elevations, *Geophysical Research Letters, 44,* 5844–5853.

Yin, J., Lin, N., Yang, Y., Pringle, W.J., Tan, J., Westerink, J.J. & Yu, D. (2021). Hazard assessment for typhoon-induced coastal flooding and inundation in Shanghai, China. *Journal of Geophysical Research: Oceans, 126(7),* e2021JC017319.

Yin, J., Jonkman, S., Lin, N., Yu, D., Aerts, J., Wilby, R., Pan, M., Wood, E., Bricker, J., Ke, Q., Zeng, Z., Zhao, Q., Ge, J. & Wang, J. (2020). Flood risks in sinking delta cities: time for a re-evaluation? *Earth's Future, 8(8),* e2020EF001614.

Figures

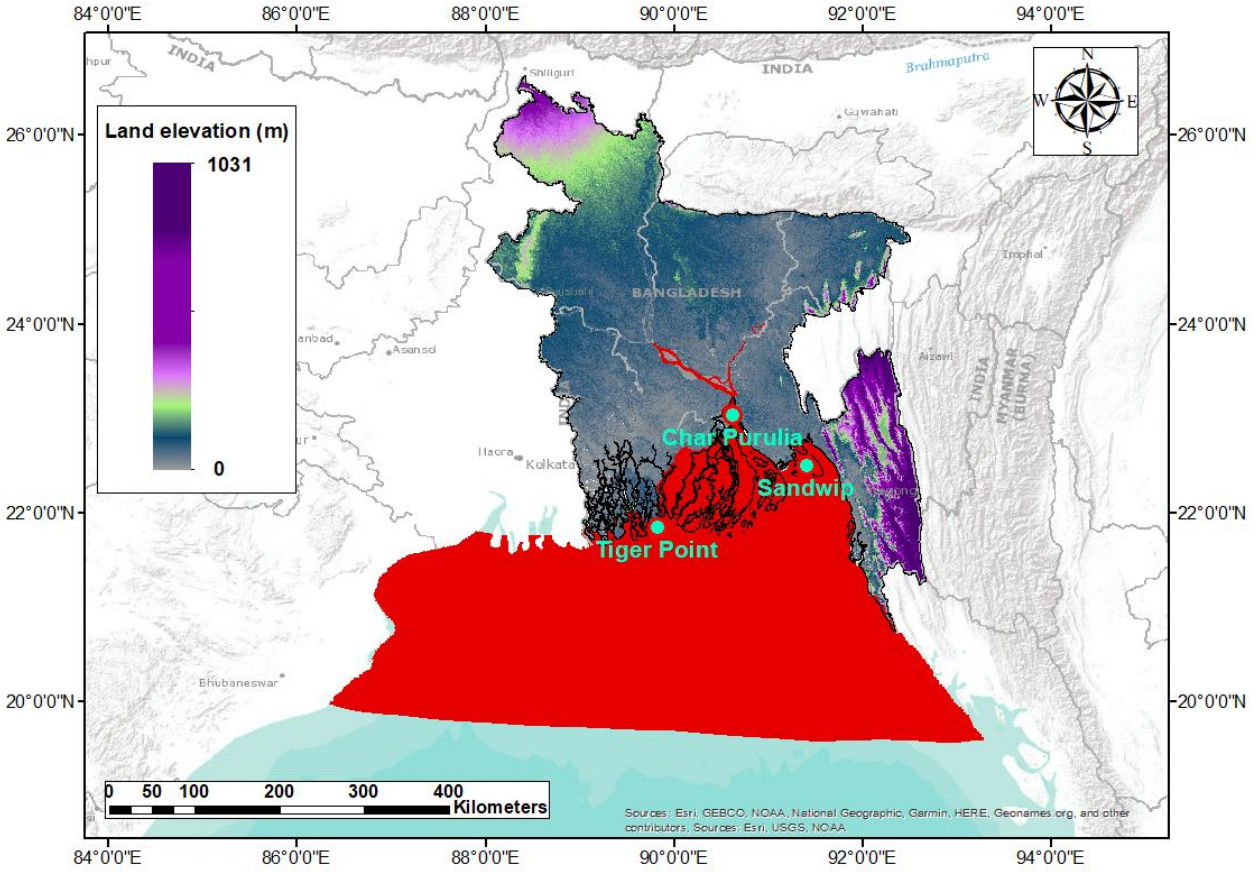

Figure 1: Map showing land elevation of Bangladesh (data downloaded from https://earthexplorer.usgs.gov/), domain of the Delft3D model used for this paper shown in red, and three locations of study – Sandwip, Tiger Point, and Char Purulia. The geographic boundary of Bangladesh is downloaded from www.geodash.gov.bd.

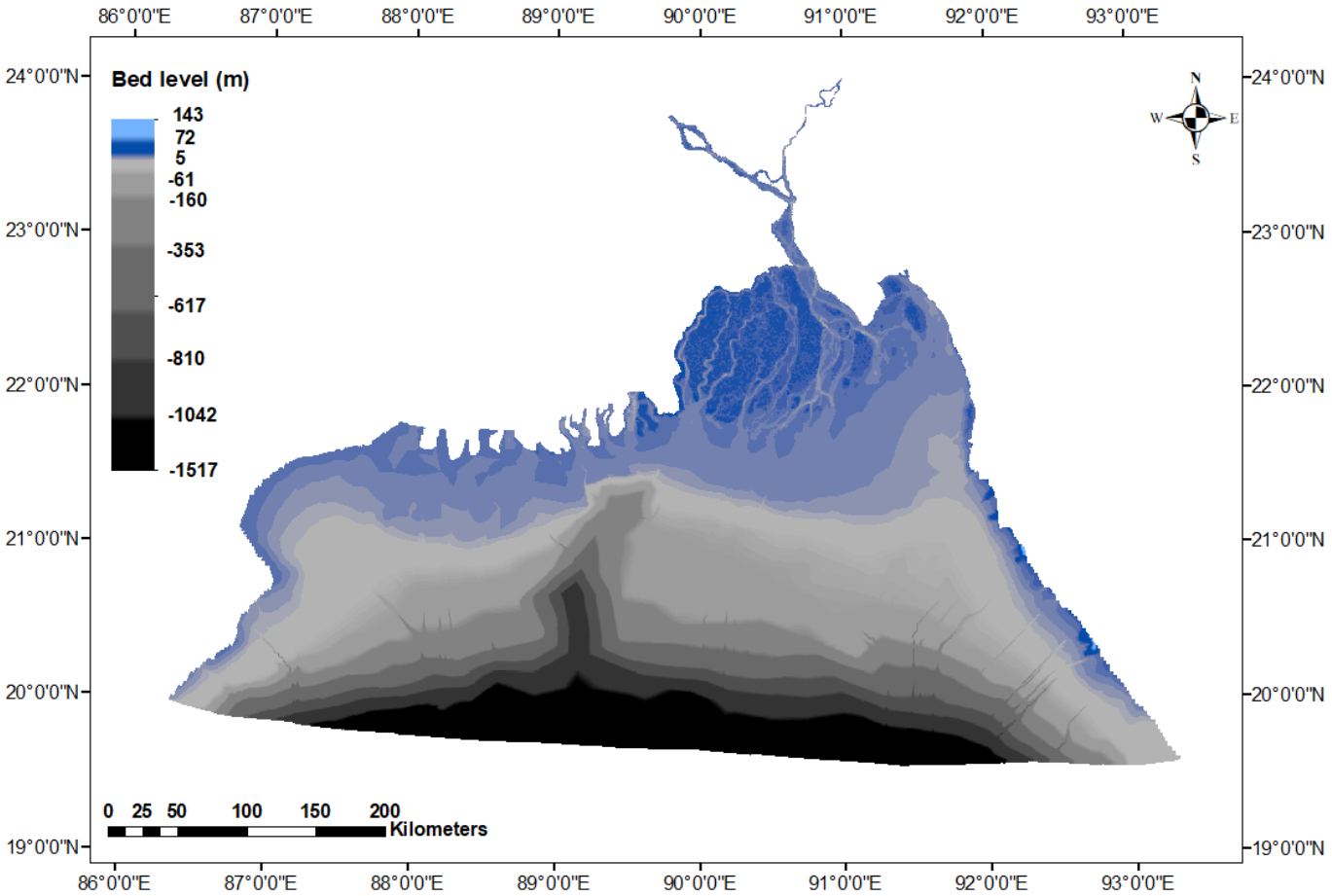

Figure 2: Model bathymetry. River bed levels (data obtained from MorphoFlood project, IHE Delft, The Netherlands) and island land elevations (downloaded from https://earthexplorer.usgs.gov/) in the Delft3D domain for the Meghna estuary and Bay of Bengal.

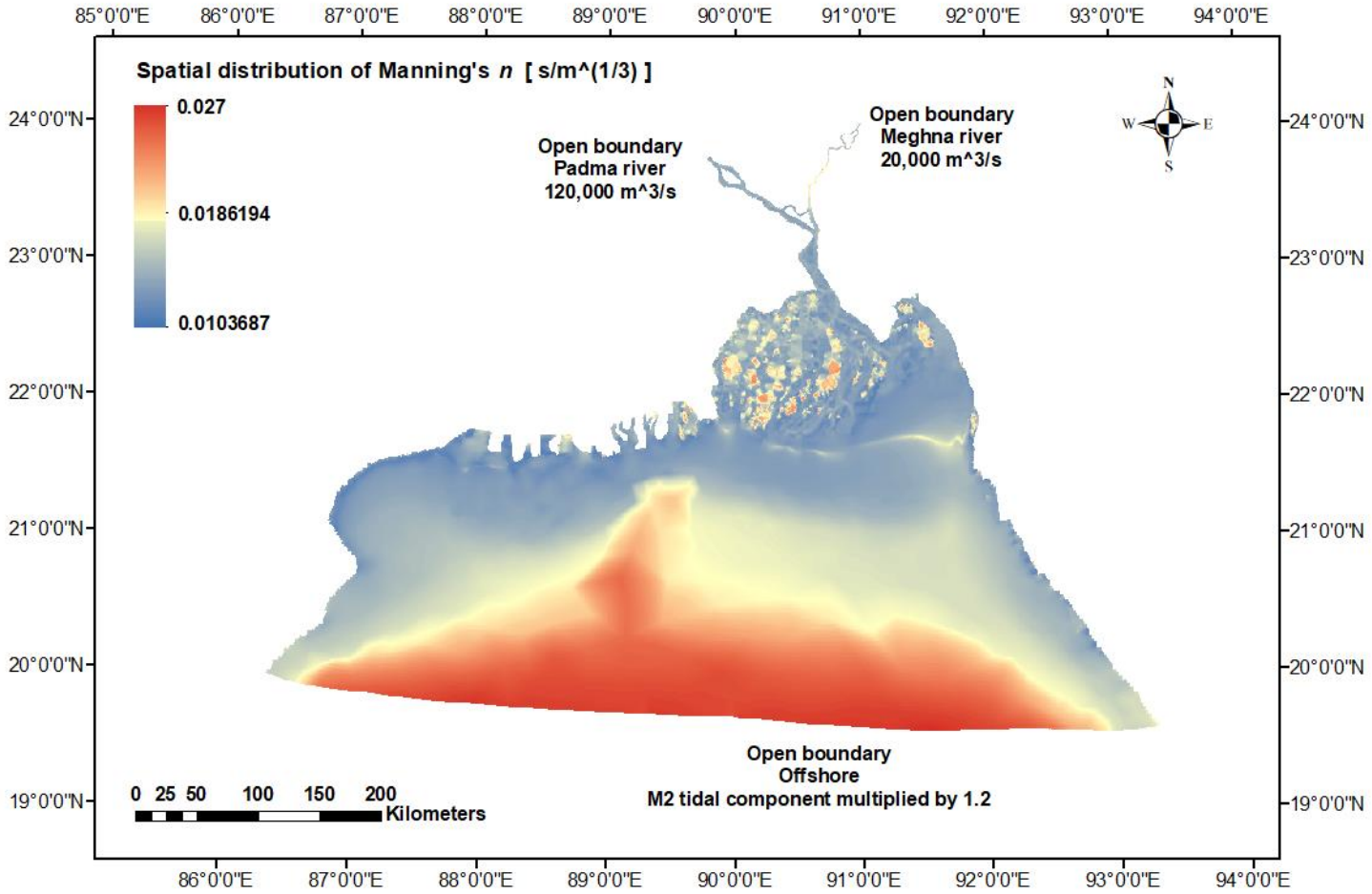

Figure 3: Spatial map of Manning's *n* calculated from Soulsby (1997) and Whitehouse et al. (2000) for the Meghna estuary and the Bay of Bengal domain (including major river tributaries). The open boundaries are also indicated.

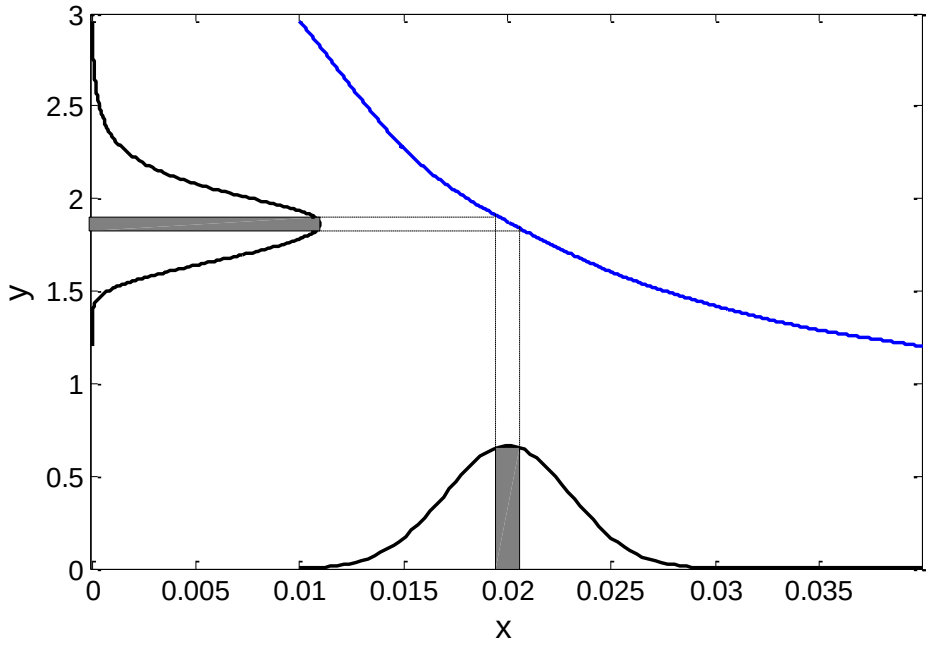

Figure 4: Probability density transfer from a PDF of *x* to a PDF of *y* through a function *y* = g(*x*).

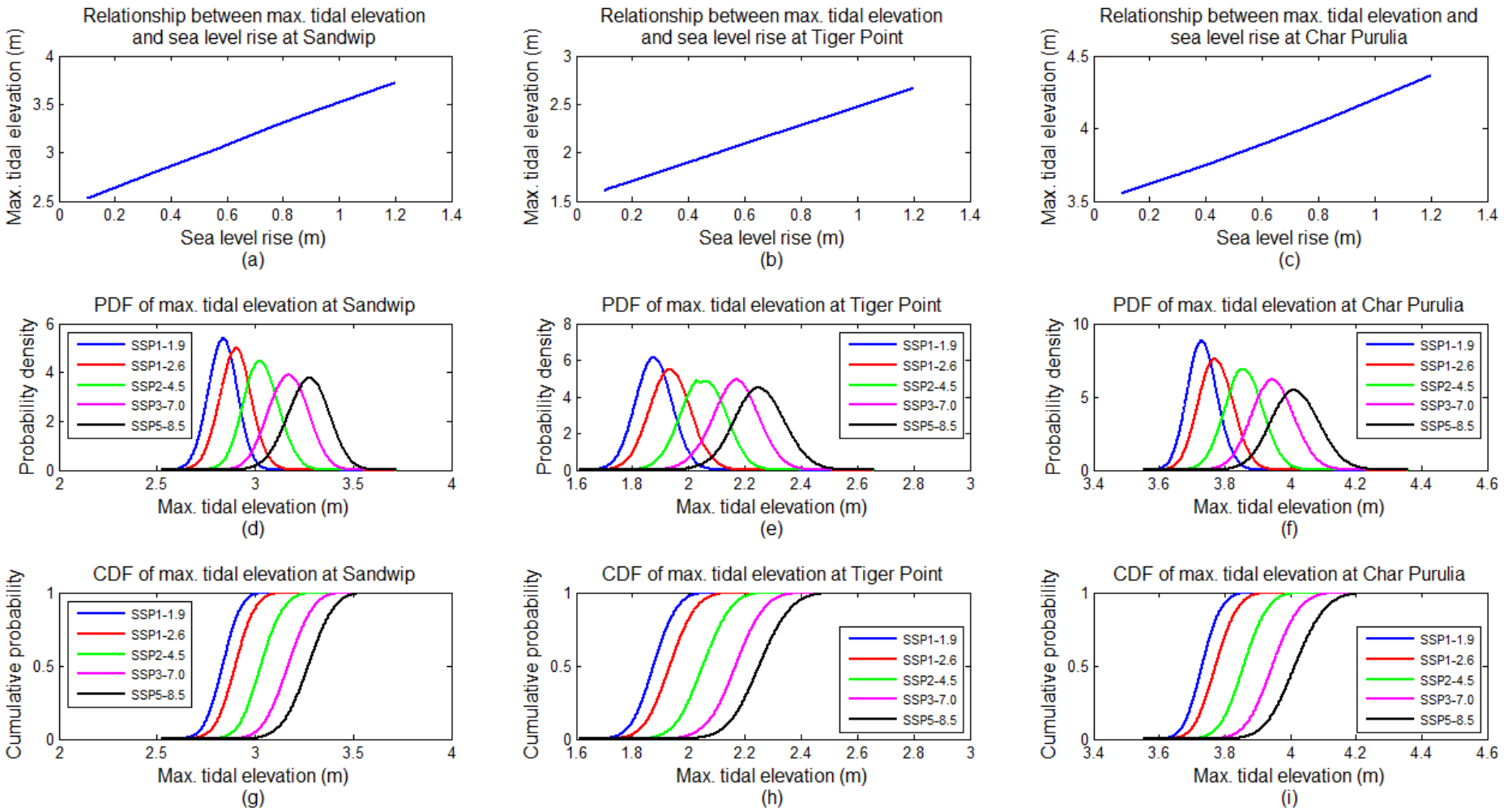

Figure 5: Relationships between maximum water level and sea level rise at (a) Sandwip, (b) Tiger Point, and (c) Char Purulia are depicted in the top row of the figure. In the middle row, (d), (e), and (f) show the derived PDFs of maximum tidal elevation for SSP1-1.9, SSP1-2.6, SSP2-4.5, SSP3-7.0 and SSP5-8.5 from IPCC 6th Assessment Report[10]. The bottom row shows the derived CDFs of maximum tidal elevation at (g) Sandwip, (h) Tiger Point and (i) Char Purulia.

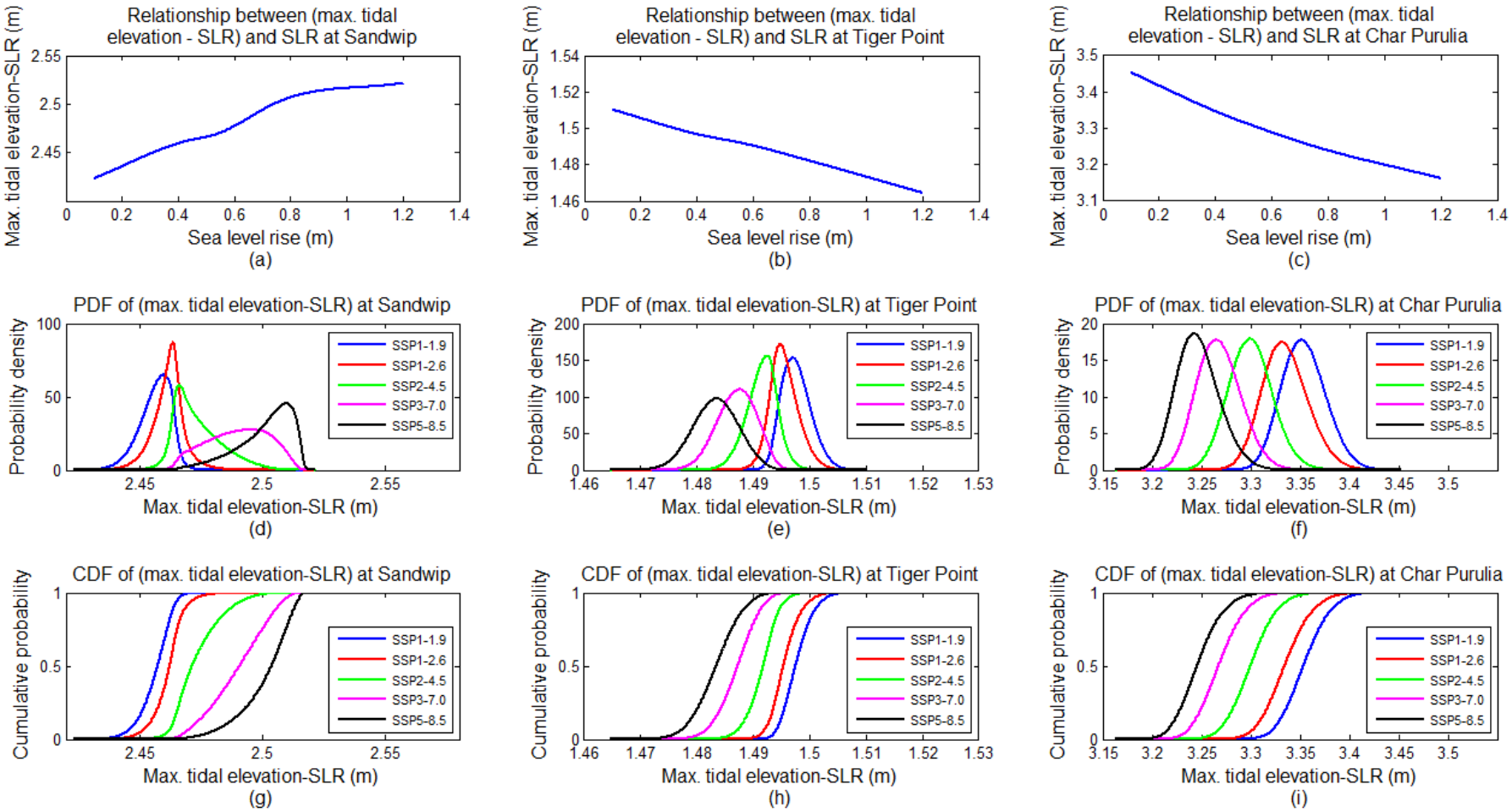

Figure 6: Relationships between maximum water level without the linear effect of sea level rise (i.e. "*s*") and sea level rise at (a) Sandwip, (b) Tiger Point, and (c) Char Purulia depicted in the top row of the figure. In the middle row, (d), (e), and (f) show the PDFs of i.e. *s* for SSP1-1.9, SSP1-2.6, SSP2-4.5, SSP3-7.0 and SSP5-8.5 from IPCC 6th Assessment Report[10]. The bottom row shows the derived CDFs of i.e. *s* at (g) Sandwip, (h) Tiger Point, and (i) Char Purulia.

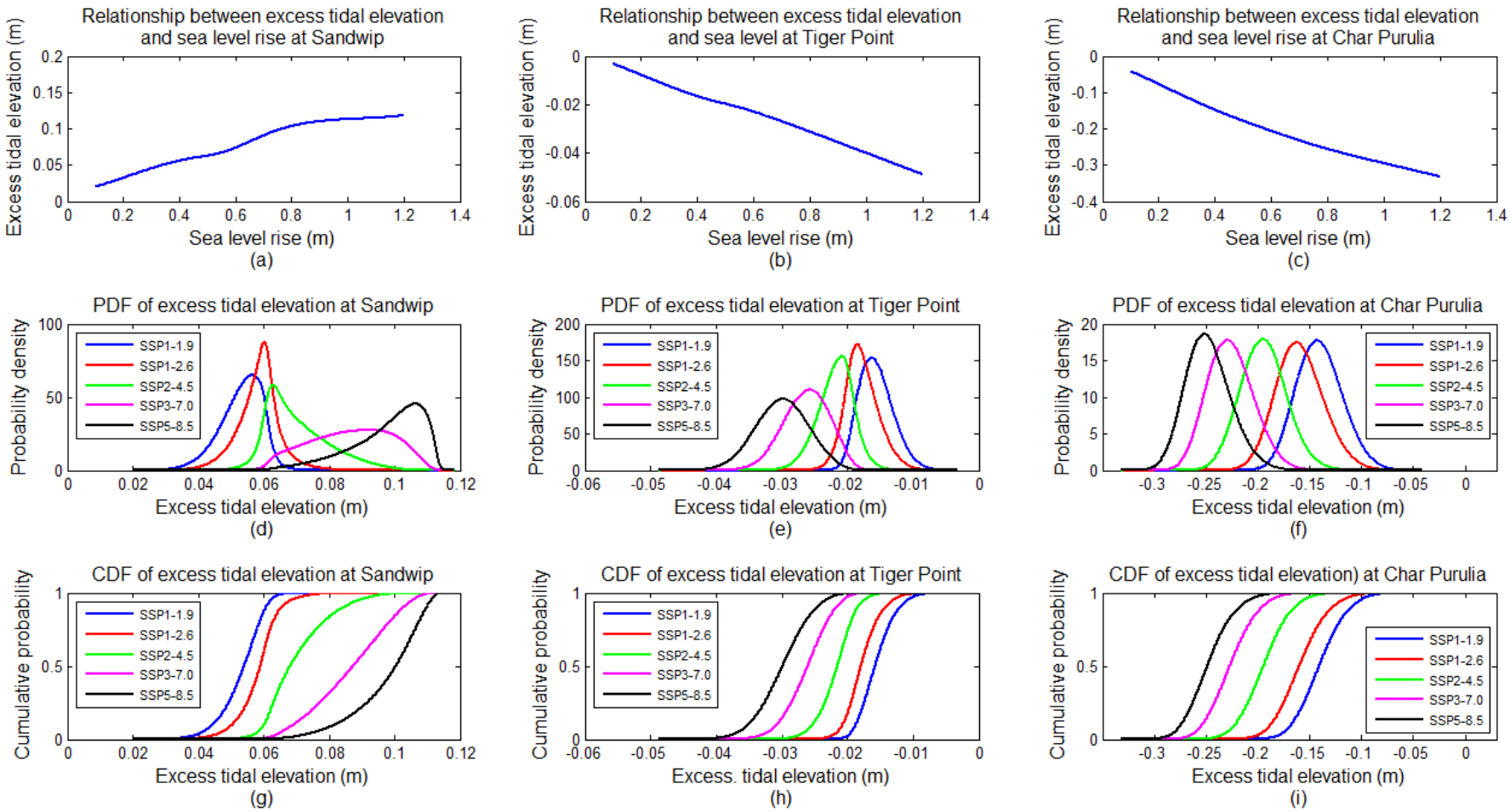

Figure 7: Relationships between excess tidal elevation (i.e., maximum tidal elevation – sea level rise – reference maximum tidal elevation) and sea level rise at (a) Sandwip, (b) Tiger Point, and (c) Char Purulia depicted in the top row of the figure. In the middle row, (d), (e), and (f) show the PDFs of excess tidal elevation for SSP1-1.9, SSP1-2.6, SSP2-4.5, SSP3-7.0 and SSP5-8.5 from IPCC 6th Assessment Assessment Report[10]. The bottom row shows the derived CDFs of excess tidal elevation at (g) Sandwip, (h) Tiger Point, and (i) Char Purulia.

Tables

Table 1: Median values and 5-95 percentile ranges for global mean sea level rise scenarios by IPCC 6th Assessment Report (Fox-Kemper et al., 2021), and the standard deviation for each scenario obtained from the 90% range.

Scenarios	Median value (m)	5-95 percentile range (m)	Standard deviation
SSP1-1.9	0.38	0.28-0.55	0.0675
SSP1-2.6	0.44	0.32-0.62	0.0750
SSP2-4.5	0.56	0.44-0.76	0.0800
SSP3-7.0	0.68	0.55-0.90	0.0875
SSP5-8.5	0.77	0.63-1.01	0.0950

Table 2: Tidal constituents at the offshore boundary

East end			West end		
Tidal constituent	Amplitude (m)	Phase	Tidal constituent	Amplitude (m)	Phase
M2	0.589	79.498º	M2	0.462	79.575º
S2	0.421	106.93º	S2	0.324	109.80º

Table 3: Expected value and other statistical moments of maximum water level, maximum water level without the linear effect of sea level rise and excess maximum water level at Sandwip, Char Purulia, and Tiger Point for five different IPCC sea level rise scenarios

				Statistical moments of maximum tidal elevation				Statistical moments of maximum tidal elevation without the linear effect of sea level rise				Statistical moments of excess maximum tidal elevation (maximum tidal elevation – sea level rise – reference maximum tidal elevation)			
Location	IPCC scenario	Mean sea level rise (m)	Standard deviation in sea level rise (m)	Expected value of max. tidal elevation (m)	Standard deviation (m)	Non-dimensional skewness	Non-dimensional kurtosis	Expected value of max. tidal elevation – sea level rise (m)	Standard deviation (m)	Non-dimensional skewness	Non-dimensional kurtosis	Expected value of max. tidal elevation – sea level rise - benchmark (m)	Standard deviation (m)	Non-dimensional skewness	Non-dimensional kurtosis
Sandwip	SSP1-1.9	0.38	0.0675	2.84	0.0739	-0.0495	3.0144	2.457	0.0065	-0.5776	3.5135	0.053	0.0065	-0.5962	3.5284
	SSP1-2.6	0.44	0.0750	2.90	0.0814	-0.0097	3.1087	2.462	0.0065	-0.0719	4.8885	0.059	0.0065	-0.0751	4.8888
	SSP2-4.5	0.56	0.0800	3.03	0.0894	0.0915	3.0014	2.474	0.0097	0.8057	3.3744	0.070	0.0097	0.8057	3.3744
	SSP3-7.0	0.68	0.0875	3.17	0.0998	-0.0235	2.8576	2.490	0.0124	-0.1697	2.1516	0.087	0.0124	-0.1697	2.1516
	SSP5-8.5	0.77	0.0950	3.27	0.1056	-0.1069	2.9519	2.501	0.0109	-0.9207	3.3283	0.098	0.0109	-0.9227	3.3308
Tiger Point	SSP1-1.9	0.38	0.0675	1.88	0.0649	0.0226	3.0086	1.4976	0.0026	0.4374	3.1541	-0.0156	0.0026	0.4083	3.1382

	SSP1-2.6	0.44	0.0750	1.93	0.0727	0.0318	3.0095	1.4955	0.0026	0.3745	3.5943	-0.0178	0.0026	0.3694	3.5917
	SSP2-4.5	0.56	0.0800	2.05	0.0781	-0.0271	2.9020	1.4915	0.0028	-0.2959	3.4479	-0.0218	0.0028	-0.2959	3.4479
	SSP3-7.0	0.68	0.0875	2.17	0.0829	-0.0565	3.0742	1.4810	0.0035	-0.2438	2.8925	-0.0263	0.0035	-0.2438	2.8925
	SSP5-8.5	0.77	0.0950	2.25	0.0895	0.0077	3.0780	1.4833	0.0040	-0.1151	2.8770	-0.0300	0.0040	-0.1185	2.8775
Char Purulia	SSP1-1.9	0.38	0.0675	3.73	0.0454	0.1180	3.0229	3.3540	0.0223	0.2103	2.9882	-0.1405	0.0223	0.2025	2.9861
	SSP1-2.6	0.44	0.0750	3.77	0.0520	0.1032	2.9673	3.3350	0.0233	0.2419	3.1141	-0.1595	0.0233	0.2406	3.1137
	SSP2-4.5	0.56	0.0800	3.86	0.0577	0.0608	2.9954	3.3000	0.0223	0.1742	3.0978	-0.1946	0.0223	0.1742	3.0978
	SSP3-7.0	0.68	0.0875	3.94	0.0653	0.0849	3.0406	3.2681	0.0222	0.2536	3.0069	-0.2264	0.0222	0.2536	3.0069
	SSP5-8.5	0.77	0.0950	4.02	0.0731	0.1003	3.0067	3.2466	0.0218	0.3321	3.1576	-0.2479	0.0218	0.3306	3.1569